Transition from nonsequential to sequential double ionization in many-electron systems

doi: 10.1103/PhysRevA.96.033401

Transition from nonsequential to sequential double ionization in many-electron systems

Michael G. Pullen,[1] Benjamin Wolter,[1] Xu Wang,[2] Xiao-Min Tong,[3] Michele Sclafani,[1] Matthias Baudisch,[1] Hugo Pires,[1] Claus Dieter Schröter,[4] Joachim Ullrich,[4,5] Thomas Pfeifer,[4] Robert Moshammer,[4] J. H. Eberly,[6] and Jens Biegert[1,7,*]

[1]*ICFO-Institut de Ciencies Fotoniques, The Barcelona Institute of Science and Technology, 08860 Castelldefels (Barcelona), Spain*

[2]*J. R. Macdonald Laboratory, Physics Department, Kansas State University, Manhattan, Kansas 66506-2604, USA*

[3]*Center for Computational Sciences, University of Tsukuba, Tsukuba 305-8577, Japan*

[4]*Max-Planck-Institut für Kernphysik, Saupfercheckweg 1, 69117 Heidelberg, Germany*

[5]*Physikalisch-Technische Bundesanstalt, Bundesallee 100, 38116 Braunschweig, Germany*

[6]*Center for Coherence and Quantum Optics, University of Rochester, Rochester, New York 14627, USA*

[7]*ICREA, Passeig Lluís Companys 23, 08010 Barcelona, Spain*

(Received 5 February 2016; revised manuscript received 19 July 2016; published 5 September 2017)

Understanding strong-field double ionization of many-electron systems is an important fundamental problem with potential implications for molecular imaging within this regime. Using mid-IR radiation, we unambiguously identify the transition from nonsequential (e, $2e$) to sequential double ionization in Xe at an intensity below 10^{14} W/cm^2. Ionization from excited orbitals is found to be decisive at low intensities, but we demonstrate that such mechanisms are unimportant in the sequential regime. We utilize these facts to successfully image a molecular dication using laser-induced electron diffraction. This methodology can be used to study molecular dynamics on unprecedented few-femtosecond time scales.

DOI: 10.1103/PhysRevA.96.033401

I. INTRODUCTION

The interaction of short ($\tau < 100$ fs) and strong laser fields ($10^{13}-10^{16}$ W/cm^2) with matter drives a continually growing range of research fields and applications. Strong-field-driven electron recollision is the basis of attosecond science [1], which aims at investigating and leveraging directly the electron pulses for techniques such as laser-induced electron diffraction (LIED) [2] or the resulting photon emission generated through the process of high-harmonic generation. The strong-field-driven electron recollision can be described by the well-known three-step model [3]: ionization of the electron near the peak of the electric field followed by acceleration and subsequent recollision with the parent ion roughly three quarters of a cycle later. Even though this model has been extremely successful, new and exciting findings continue to be uncovered that help to further develop [4,5], and in some cases seriously challenge [6], theoretical interpretations.

II. BACKGROUND

One aspect of strong-field physics that continues to provide many insights is double ionization (DI). Early experiments showed that the detected yield of doubly charged ions below the saturation threshold for ionization was much higher than expected from two sequential tunneling events [7]. The electrons contributing to this unexpectedly higher yield therefore originate from a "nonsequential" double-ionization (NSDI) process. The NSDI region is intricately linked to the recollision of the first electron (e_1) and can proceed via two routes: Either the second electron (e_2) can be directly ionized by e_1 via the so-called (e, $2e$) mechanism, or it can be resonantly excited by e_1 and subsequently tunnel ionized at a later time (RESI). Double ionization is a complex process that is known to be dependent on a number of laser parameters such as the intensity [8,9], polarization [10], pulse duration [11], and wavelength [12,13]. NSDI is observed below the saturation intensity I_S, which is the point where sequential double ionization (SDI) starts to dominate, and seems to be ubiquitous in low-Z atomic targets [14] and small molecules [15]. Interestingly, in the case of high-Z atoms (Z is nuclear charge) such as Xe, which is one of the most well studied atomic species, the understanding of DI is not as clear [16]. In the near-IR ($0.8\ \mu\text{m} < \lambda < 3\ \mu\text{m}$) wavelength regime different enhancement mechanisms such as multiple-electron recollisions [12,17] and resonant excitations [16–18] have been proposed to explain the disparate results. Nowadays, it is generally accepted that ion yield measurements alone are not sufficient to unambiguously determine the regime of DI. Additional measurements of the doubly charged ion momentum distribution [9,19] or electron correlations [20] are required. The most sophisticated investigation of DI in Xe utilized these techniques and showed that, unlike low-Z targets, the results were suggestive of SDI at the low peak intensities where NSDI normally dominates [21]. Screening of the valence electrons by core electrons was proposed to explain the surprising results.

It is often beneficial to scale experiments to longer wavelengths where classical methods can accurately describe the tunneling regime interaction. Two results have been reported for which the goal was to investigate DI in Xe at longer wavelengths [22,23]. Gingras *et al.* explored a wide wavelength range while monitoring single- and double-ion yields as a function of the laser intensity. In addition to supporting the idea of resonances at shorter wavelengths, there was evidence for the occurrence of NSDI at longer wavelengths. The position of the famous "knee structure", which is traditionally near the meeting point of SDI and other mechanisms, was observed below 10^{14} W/cm^2 as the wavelength was increased towards 2 μm. These results suggest that SDI should already become dominant below 10^{14} W/cm^2 in the mid-IR ($\lambda > 3\ \mu$m). Interestingly, this expectation was

*jens.biegert@icfo.eu

not observed at wavelengths of 3.2 and 3.6 μm, where the measured yields for DI could still be described using inelastic electron impact cross sections [23]. Neither of the above reports included doubly charged ion momentum distributions or electron correlation maps. Therefore, no single experiment has unambiguously shown the transition from NSDI to SDI in Xe, and there is still much uncertainty and debate as to the mechanisms of DI in high-Z targets.

Here, using ion yields, ion momenta, and electron correlations as a function of peak intensity, we perform a thorough investigation into the DI of Xe in the mid-IR regime and unambiguously identify the transition from $(e, 2e)$ NSDI to SDI. By comparing our experimental results with semiclassical calculations, we show that SDI starts to dominate over the $(e, 2e)$ mechanism well below $10^{14}\,\mathrm{W/cm^2}$, which is at odds with previous reports. A comparison with time-dependent density-functional theory (TDDFT) also shows that the $5s5p^6$ orbital [12,18,22] plays an important role during NSDI at intensities close to $10^{13}\,\mathrm{W/cm^2}$. These results suggest that important mechanisms that were previously observed in the near IR and that would complicate LIED imaging within the DI regime, are not important during SDI in the mid-IR. Using the molecule acetylene (C_2H_2) as an example, we successfully demonstrate the extraction of geometrical structure from a molecular dication by applying the LIED technique within the SDI regime. This methodology will be important for future investigations of molecular dynamics at unprecedented time scales.

III. THEORY

Our theoretical investigation is based on both, semiclassical and TDDFT calculations. The TDDFT approach solves the time-dependent Kohn-Sham equations [24] with the Hamiltonian written as

$$H(\boldsymbol{r},t) = -\tfrac{1}{2}\nabla^2 + V_{\mathrm{eff}}^{\mathrm{PP}}[\,\rho(\boldsymbol{r},t)] + V_{\mathrm{ext}}(\boldsymbol{r},t),$$

where $V_{\mathrm{ext}}(\boldsymbol{r},t)$ is the electron-laser interaction and $V_{\mathrm{eff}}^{\mathrm{PP}}[\,\rho(\boldsymbol{r},t)]$ is the nonlocal ℓ-dependent pseudopotential as detailed in Ref. [25]. To analyze the electron-electron dynamic effect, we further recast $V_{\mathrm{eff}}^{\mathrm{PP}}[\,\rho(\boldsymbol{r},t)]$ into

$$V_{\mathrm{eff}}^{\mathrm{PP}}[\,\rho(\boldsymbol{r},t)] = V_{\mathrm{eff}}^{\mathrm{PP}}[\rho_0(\boldsymbol{r})] + \left\{V_{\mathrm{eff}}^{\mathrm{PP}}[\,\rho(\boldsymbol{r},t)] - V_{\mathrm{eff}}^{\mathrm{PP}}[\rho_0(\boldsymbol{r})\,]\right\}, \tag{1}$$

two terms, with $\rho_0(r)$ being the laser field-free electron density and $\rho(\boldsymbol{r},t)$ being the time-dependent electron density. The first term represents the single active electron potential, and $\{V_{\mathrm{eff}}^{\mathrm{PP}}[\,\rho(\boldsymbol{r},t)] - V_{\mathrm{eff}}^{\mathrm{PP}}[\rho_0(\boldsymbol{r})\,]\}$ stands for the electron-electron dynamic effect. Note that the dominant contribution to the second term is the Coulomb interaction due to the density changes. To compensate the spurious self-interaction [26], we added a positive charge background $\rho_+(r) = \frac{c^3}{2}e^{-cr}$, which provides the correct Coulomb tail. We choose $c = 0.122$, with which the ionization potential from the simulation is 12.13 eV, close to the measured one. We solved the time-dependent equation using the generalized pseudospectral method in the energy representation [27] and project out the time-dependent wave function in the outer region onto the momentum space, as detailed in Ref. [28]. When the laser pulse is over, we obtain the ionization probability p_i for each orbital. In the simulation, we included all eight valence electrons (two $5s$ states, $i = 1$, 2, and six $5p$ states, $i = 3,4, \ldots, 8$). As we know and also confirmed in Ref. [23], the contribution of the $5s$ states to the single ionization is negligible. As shown in Ref. [25] for the Ar case, if we turn off the electron-electron dynamical correlation [set the second term in Eq. (1)] in the simulation, the ionization probability of $3s$ is about 4 orders smaller than the one with the term. Therefore, we conclude that for the present case, the $5s$ state is mainly ionized through electron-electron dynamical correlation or rescattering reduced ionization, not direct laser field ionization, and its contribution should directly add to the double ionization, not the single ionization. Thus, we define the double-ionization probability with the $5s$ contribution as

$$P_{5s}^{++} = P^{++} + 2p_{5s}(1 - p_{5s})\prod_{k=3}^{8}(1 - p_k).$$

Another reason to add the $5s$ contribution to the double ionization is that even if there is a $5s$ single-ionization state created by the laser field directly, the $5s$ hole will be filled by a laser-enabled Auger decay process [29,30], which results in the double ionization.

The semiclassical method assumes quantum tunneling of the first electron e_1. For each time step, a tunneling rate $w(t)$ is calculated according to the Ammosov-Delone-Krainov tunneling formula [31,32]

$$w(t) = \frac{C_l^2}{2^{|m|}|m|!}\frac{(2l+1)(l+|m|)!}{2(l-|m|)!}\frac{1}{\kappa^{\frac{2Z_c}{\kappa}-1}}\left(\frac{2\kappa^3}{|E(t)|}\right)^{\frac{2Z_c}{\kappa}-|m|-1} \times e^{-2\kappa^3/3|E(t)|},$$

where l and m are the quantum numbers of the orbital from which the electron is tunneled out (for Xe $5p$, $l = 1$ and $m = 0$), the coefficient $C_l = 2.57$ is found in Ref. [33], $\kappa = \sqrt{2I_{p1}}$, with $I_{p1} = 12.13$ eV being the first ionization potential of Xe, and $Z_c = 1$ a.u. is the effective charge of the ion core.

The tunneling exit point, which is also the initial position of e_1, is determined in parabolic coordinates [34,35] via numerically solving the following equation:

$$-\frac{\beta_2}{2\eta} + \frac{m^2-1}{8\eta^2} - \frac{E(t)\eta}{8} = -\frac{I_{p1}}{4},$$

where β_2 is a separation constant and η is a variable of the parabolic coordinates to be solved. The tunneling exit point in the Cartesian coordinates is then given by $z_0 = -\frac{\eta}{2}\mathrm{sgn}[E(t)]$, assuming the laser polarization is along the z direction. Note that $\eta \geqslant 0$. If $E(t) > 0$, then tunneling is to the negative z direction, and if $E(t) < 0$, then tunneling is to the positive z direction. The velocity of the first electron at the tunneling exit is assumed to be zero.

Having set the birthplace and velocity of the first electron, let us turn to the second electron. The second electron is "created" in the vicinity of the ion core, which has a charge of +2 a.u. The procedure of assigning e_2 a position and a momentum is described as follows. First, a position is randomly assigned, and the potential energy of e_2 is calculated, denoted E_{p2}, which includes the ion-core attraction energy and the $e-e$ repulsion energy. If $E_{p2} > -I_{p2} = -20.98$ eV (the second ionization potential of Xe), this position is rejected, and a new position is assigned until the classically allowed

condition $E_{p2} < -I_{p2}$ is fulfilled. Then the kinetic energy of the second electron is given by $E_{k2} = -I_{p2} - E_{p2} > 0$. With this kinetic energy, the three momentum components of e_2 are randomly partitioned.

Now we have assigned the initial positions and momenta of both electrons. Remember that we are currently at time t during the pulse. From this time t until the end of the pulse, the motion of the two electrons is governed by classical mechanics via numerically integrating the time-dependent Newtonian equation of motion

$$\frac{d^2\vec{r_i}}{dt^2} = -\vec{\nabla}[V_{ne}(r_i) + V_{ee}(r_{12})] - \hat{z}E(t), \quad i = 1,2,$$

where $\vec{r_i}$ is the position of the ith electron, $r_{12} = |\vec{r_1} - \vec{r_2}|$ is the distance between the two electrons, $V_{ne}(r_i) = -2/r_i$ is the nuclear-electron Coulomb potential, and $V_{ee}(r_{12}) = 1/r_{12}$ is the electron-electron Coulomb potential. The trajectories (i.e., positions and momenta) of the two electrons are followed and recorded from the birth time t to the end of the pulse. A double-ionization event happens if, at the end of the pulse, both electrons have positive energies.

The weight of a two-electron trajectory can be given by $p(t) = w(t)\Delta t$ for low intensities where the total ionization probability by the entire pulse is small. For relatively high intensities where the total ionization probability is not small so that the population of the neutral atoms is depleted appreciably during the pulse, the weight should be modified to $p(t) = N(t)w(t)\Delta t$, where $N(t) = \exp[-\int_{-\infty}^{t} w(t')dt']$ is the survival probability of neutral atoms at time t. The probability of double ionization is obtained by summing the weights of all double-ionization events at the end of the pulse. Postselecting these double-ionization events, we can trace back the trajectories of the two electrons during the pulse.

Intensities below 4×10^{13} W/cm^2 cannot be investigated with this method due to computational demands. The TDDFT method utilizes pseudopotentials [25], and to compensate spurious self-interaction a positive-charge background is added [26], which provides the correct Coulomb tail. Ionization from the excited Xe$^+$ $5s5p^6$ orbital can optionally be included in the calculation. Simulations suggest this state is accessed via electron-rescattering-induced excitation and not via multiphoton resonances [12,18].

IV. RESULTS

For the experimental investigation, we ionize Xe with a highly stable (1% rms fluctuations over 12 h) and intense 160-kHz mid-IR source that operates at a wavelength of 3.1 μm [36] and is thus well suited to explore strong-field physics [37]. Upon focusing using a 50-mm focal-length mirror, intensities above 10^{14} W/cm^2 can be achieved. The focused radiation intersects a cold beam of atomic Xe that has passed two skimming stages into a reaction microscope (ReMi) spectrometer [38], which has a base pressure below 10^{-10} mbar without gas load. The laser polarization direction is parallel to the electric and magnetic fields of the ReMi spectrometer, which means that longitudinal momentum information can be directly inferred from time-of-flight (TOF) spectra.

In Fig. 1(a) we present the results of monitoring Xe$^+$ – Xe^{4+} ion yields as a function of the peak intensity. The single-ionization (circles) data show the typical saturationlike behavior as the intensity is increased towards $I_S \sim 5.0 \times 10^{13}$ W/cm^2 [39]. The doubly charged ion (squares) data show a similar gradient for intensities below I_S, as is generally observed in the NSDI regime [40]. Rescaled single-ionization data (black curve) clearly illustrate this similarity. Approaching I_S the NSDI yield begins to plateau in a way similar to the single-ion yield due to the lack of neutral atoms in the interaction volume [15]. At intensities higher than I_S, however, the Xe^{2+} yield starts to increase again, and this trend continues up until the maximum intensity of 1.2×10^{14} W/cm^2. Such a pronounced change in the intensity dependence of the ion yield is characteristic of the transition from NSDI to SDI [40]. The yields of the triple and quadruple charged ions (triangles and diamonds, respectively) do not show this trend. The increase

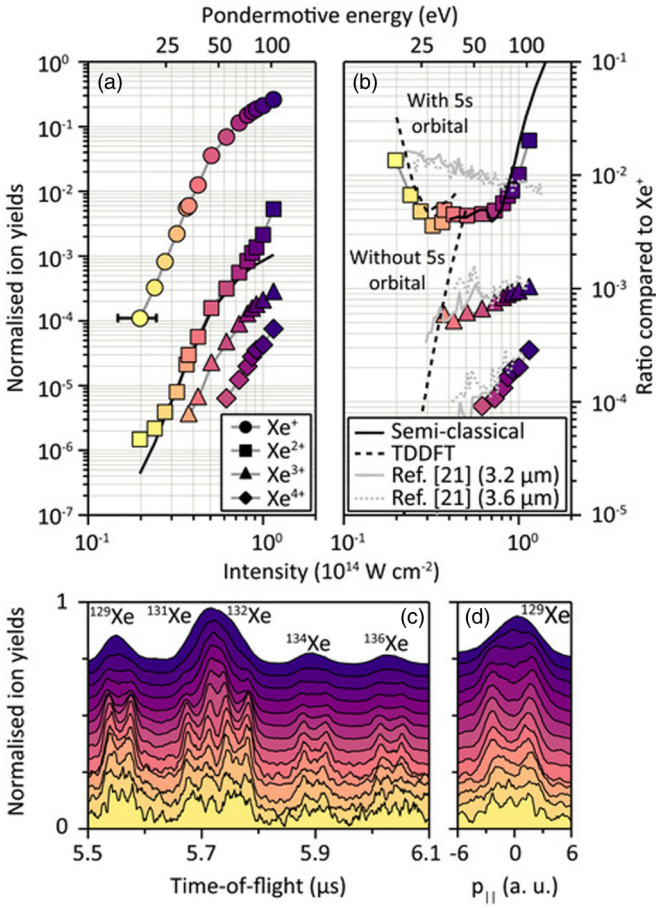

FIG. 1. (a) The number of Xe$^+$ (circles), Xe^{2+} (squares), Xe^{3+} (triangles), and Xe^{4+} (diamonds) ions detected as a function of the estimated peak laser intensity. The Xe$^+$ data are also scaled to overlap with the Xe^{2+} curve at intermediate intensities (black line). The estimated ±20% error in the absolute intensity determination is indicated on the first Xe$^+$ data point. (b) The corresponding ion yield ratios shown alongside the semiclassical (solid black line) and TDDFT (dashed black line) calculations. The data from Ref. [23] acquired for similar wavelength (solid and dashed gray lines) are shown for comparison. Normalized and vertically shifted (c) TOF spectra for five Xe double-ion isotopes and (d) momentum distributions for ^{129}Xe^{2+} as the intensity is increased from bottom to top.

in Xe^{2+} counts is more obvious when viewed as a ratio of doubly to singly charged ion yield, as presented in Fig. 1(b) (squares). A plateau at a value between 4×10^{-3} and 5×10^{-3} is observed up until I_S, upon which the ratio starts to increase drastically. We note that while the Xe^{3+} and Xe^{4+} data reported in Ref. [23] for similar wavelengths [shown in Fig. 1(b) as gray solid and dashed lines for comparison] agree well with our observations, the trend in doubly to singly charged ion yield ratio definitively does not. The reason for this is not clear, but it could be related to the intensity calibration, the accuracy of which is generally limited to the tens of percent level or worse [41].

V. DISCUSSION

The semiclassical calculations (solid black), which have been rescaled by a factor of 0.3 to compensate for the absence of focal averaging, reproduce both the plateau and the gradient of the Xe^{2+}/Xe^{+} ratio above I_S. This comparison clearly shows that DI in the mid-IR regime can be accurately modeled using semiclassical methods. The TDDFT results for intensities between 2×10^{13} and 5×10^{13} W/cm^2 are also presented (dashed black line) and emphasize the decisive role of the $5s5p^6$ orbital for NSDI in the mid-IR regime: The calculations that include the $5s5p^6$ orbital accurately reproduce the change in ratio observed for lower intensities.

The evolution of the TOF spectra of Xe^{2+} ions with increasing intensity is presented in Fig. 1(c). Each spectrum contains five isotopes and is normalized before being vertically shifted for visibility. Apart from the lowest intensity, a clear transition from a double-peak structure at low intensities (bottom traces) to a single peak at high intensities (upper traces) is observed for each isotope. The calculated ion momenta for $^{129}Xe^{2+}$ are shown in Fig. 1(d). The double-peak structure is suggestive of the $(e, 2e)$ NSDI mechanism where the doubly charged ion is created at a phase close to the zero crossing of the electric field, yielding a large drift momentum [9]. To the best of our knowledge, a double-hump structure in the Xe^{2+} momentum distribution has never been reported in the literature. The results seem to rule out an influence of the RESI and resonant enhancement mechanisms as both are known to "fill the valley" between the double hump [9,21]. The absence of these mechanisms is not unexpected since (1) RESI dominates when the returning electron energies are large enough to excite the ion but too low for impact ionization, which is not the case here, and (2) the contribution from resonant enhancement decreases with increasing wavelength [22]. The narrowing of the ion momentum distributions as the intensity is increased indicates a convergence towards purely sequential ionization [9]. The same analysis of the Xe^{3+} TOF (not presented here) spectra shows that the double-hump behavior persists at the highest intensity, which indicates that nonsequential ionization is still the dominant mechanism for creating triply charged ions.

The excellent agreement of the semiclassical ratios in Fig. 1(b) with experiment provides confidence that all interaction mechanisms are captured and thus opens up the ability to track the individual electron trajectories in order to get further insights. In Figs. 2(a) and 2(b), we present representative trajectories for both ionized electrons for intensities of 4.0×10^{13} and 1.2×10^{14} W/cm^2. For the lower intensity, we see that e_1 (dotted purple line) is emitted at the peak of the pulse ($t = 0$ cycles) and is able to directly impact ionize e_2 (solid yellow line) upon returning to the core. This is a typical example of $(e, 2e)$ DI where e_2 is directly ionized upon recollision and the two electrons show correlated behavior by leaving in the same direction. The fact that the experimental results can be reproduced without including excitations or resonances confirms that these mechanisms are not important in this regime. The motions of the two electrons at the higher intensity are tellingly different. Due to the much higher intensity, e_1 can be emitted much before the peak intensity and does not at all return to the vicinity of the core. For e_2 to also be emitted it must undergo a sequential ionization process, in which case little correlation between the two electrons is expected. Interestingly, in this example e_2 returns to the vicinity of the parent dication half a cycle later.

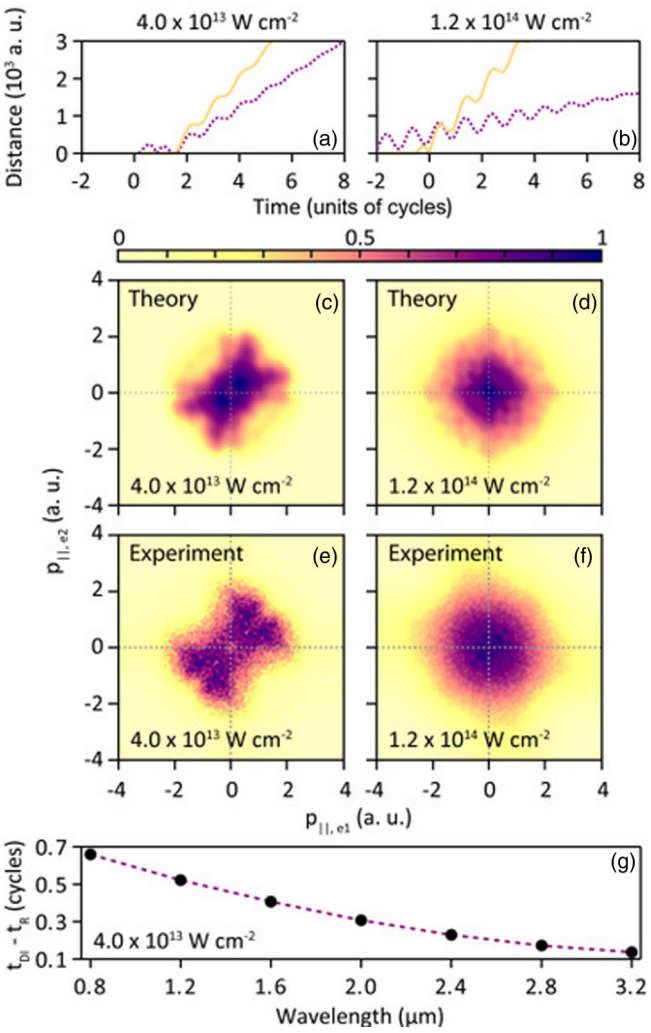

FIG. 2. (a) and (b) Example first (dotted purple line) and second (solid yellow line) electron trajectories for intensities of 4.0×10^{13} W/cm^2 (left column) and 1.2×10^{14} W/cm^2 (right column). (c) and (d) Simulated electron correlation maps. (e) and (f) Experimentally measured electron correlation maps. (g) Time difference between the return of e_1 and the ionization of e_2 as a function of wavelength at an intensity of 4.0×10^{13} W/cm^2.

Correlations between e_1 and e_2 can be deduced by comparing their theoretical [Figs. 2(c) and 2(d)] and experimental [Figs. 2(e) and 2(f)] longitudinal momenta. The experimental correlation data are associated with only the $^{129}Xe^{2+}$ isotope and were symmetrized along the $p_{||,e2} = p_{||,e1}$ and $p_{||,e2} = -p_{||,e1}$ diagonals. For the lower intensity, both show a pronounced correlation in the first and third quadrants. A forklike structure is observed along the diagonal for both experiment and theory, indicating the excellent agreement between the two. It is interesting to note that both show counts in the second and fourth quadrants as well, which indicates that there is a small amount of anticorrelated electron emission. These results are distinctly different from a recent experiment in which no correlations were found for any of the investigated intensities at the 790-nm wavelength [21]. In fact, apart from some initial evidence presented by our group [37], the observation of electron correlations during DI of Xe does not seem to exist in the literature. For the higher intensity, no evidence of electron correlations is present in either the experiment or simulations, indicating that this intensity is well within the SDI regime. In Fig. 2(g) we present the difference between the rescattering time of $e_1(t_R)$ and the ionization time of $e_2(t_{DI})$ for a constant intensity of 4×10^{13} W/cm^2. Larger time differences are an indication of the RESI mechanism, while smaller time differences are indicative of $(e, 2e)$ DI. Increasing the wavelength results in a dominance of the $(e, 2e)$ mechanism. This can be understood in terms of an increasing ponderomotive energy, which is proportional to the square of the wavelength, and therefore return energies greater than the second ionization potential being more readily generated.

The results in Fig. 2 show that the trajectories of both electrons resulting from DI in the mid-IR regime can be accurately modeled using a simple classical approach [38]. This means that any elastic rescattering event that occurs during SDI in the mid-IR can be interpreted classically as in LIED [39]. If the omnipresent fragmentation processes that accompany molecular ionization occur in the SDI regime, then they can potentially be imaged using the LIED technique. In Fig. 3(a) we present acetylene (C_2H_2) ion yield ratios as a function of the laser intensity. The $C_2H_2^{2+}/C_2H_2^+$ trend (circles) is very similar to the Xe case, suggesting the dominance of SDI at intensities above $I_S \sim 4 \times 10^{13}$ W/cm^2. The decrease in I_S relative to Xe is due to the 0.7 eV lower ionization potential. To confirm the SDI mechanism in Fig. 3(b) we show how the $C_2H_2^{2+}$ longitudinal momentum distribution evolves from a double-peak structure into a single peak as the intensity is increased.

Using a laser intensity of 6.5×10^{13} W/cm^2 and therefore under the assumption of SDI from the neutral C_2H_2 ground state, we have analyzed the associate electron momentum distribution using the LIED technique [42] and extracted bond lengths that are consistent with the expected values [43]. Here, according to quantitative rescattering (QRS) theory [6], we are able to extract the field-free differential cross section (DCS) of electrons that return to the parent dication, in the present case with an energy of 50 eV, by compensating for the vector potential that is acquired by the electrons upon return. The structural information of the molecular dication can then be determined from the molecular contrast factor (MCF), which is calculated by comparing this molecular

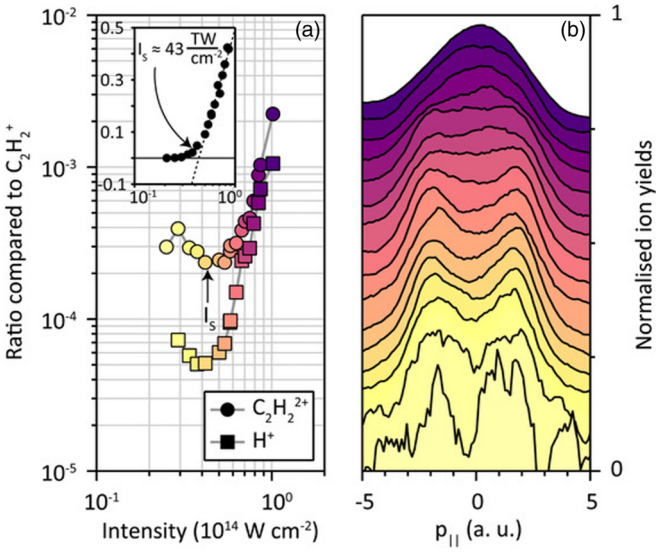

FIG. 3. (a) The experimental $C_2H_2^{2+}/C_2H_2^+$ (circles) and $H^+/C_2H_2^+$ (squares) ratios as a function of the estimated peak intensity. (b) Normalized and vertically shifted $C_2H_2^{2+}$ ion momentum distributions for increasing intensity from bottom to top.

DCS with its theoretical analogue. The MCF contains the molecular structure at the time of the electron's return. In order to extract the experimentally measured positions of the individual nuclei, theoretical MCFs are computed for a range of C-C and C-H distances and compared with the experimental MCF, and a minimization routine extracts the best match (a detailed description is given in Ref. [42]). In Fig. 4(a) the corresponding χ^2 fitting results are shown for antialigned acetylene molecules. The minimum χ^2_{min} value is found (red point) for C-C and C-H bond lengths of 1.28 ± 0.33 and 1.32 ± 0.37 Å, respectively. In Fig. 4(b) the corresponding fitted MCF (red line) is shown with the experimental MCF (black dots). Due to the lower probability of double ionization compared to single ionization, the data are noisier than in Pullen *et al.* [42]. The lower signal is also reflected in the large bond-length error bars. This result indicates a stretch of both C-C and C-H

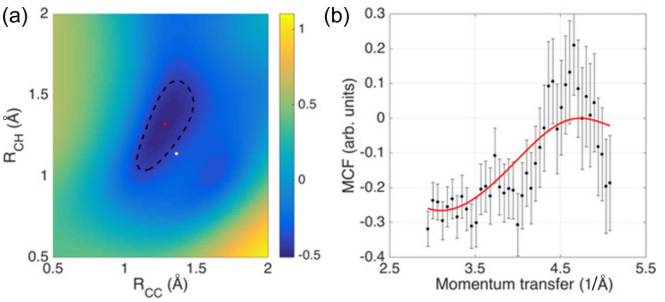

FIG. 4. The results of analyzing the acetylene dication geometry using the LIED method. (a) The χ^2 fitting results showing a minimum (χ^2_{min}) at bond lengths of $R_{CC} = 1.28 \pm 0.33$ Å and $R_{CH} = 1.32 \pm 0.37$ Å. The dashed black contour is at the $1.5\chi^2_{min}$ level and is used to define the error bars. The white data point represents the expected dication equilibrium structure. (b) The molecular contrast factor (MCF; black data points) and the best fit (red curve). This fit is used to determine the molecular structure.

bond lengths of the acetylene dication ground state compared to the structure of the neutral molecule. The expected dication equilibrium structure (white dot) is given in [43] as 1.137 Å (C-H) and 1.362 Å (C-C), which lies close to the 50% level (black dashed line) of our experimentally extracted χ^2_{min} value.

To highlight the potential for using this method to image dynamics, we show that the fast C_2H_2 deprotonation channel ($C_2H_2{}^{2+} \rightarrow H^+ + C_2H^+$) [44] also displays characteristics of sequential behavior (squares) at intensities near $\sim 3 \times 10^{13}$–4×10^{13} W/cm^2 [squares in Fig. 3(a)]. We have confirmed that the majority of the H+ counts result from dissociation of the dication and not the dissociation of the cation by performing a coincidence measurement at an intensity of 6×10^{13} W/cm^2. Therefore, ultrafast fragmentation processes such as deprotonation from $C_2H_2{}^{2+}$ excited states, which cannot be temporally resolved using other imaging techniques due to their few-femtosecond nature, can be imaged by taking advantage of SDI within the mid-IR wavelength regime. Recently, we have demonstrated the feasibility of this approach by imaging the deprotonation channel of C_2H_2 [45].

VI. CONCLUSION

Summarizing, we have shown that strong-field ionization of Xe in the mid-IR progresses from NSDI via the $(e, 2e)$ mechanism at intensities near 10^{13} W/cm^2 to SDI as the intensity is increased towards 10^{14} W/cm^2. This result contradicts previous reports and shows that mechanisms that have previously been shown to be important at shorter wavelengths become negligible in the mid-IR. The influence of the $5s5p^6$ orbital is shown to influence the NSDI yield dramatically at intensities close to 10^{13} W/cm^2. We also show how SDI in the mid-IR could be utilized to image few-femtosecond molecular fragmentation dynamics using the LIED technique. This possibility is extremely enticing as it represents the possibility to image molecular fragmentation channels on time scales that are unprecedented when using other imaging methods.

ACKNOWLEDGMENTS

We acknowledge financial support from the Spanish Ministry of Economy and Competitiveness through Grant No. FIS2014-56774-R, the "Severo Ochoa" Programme for Centres of Excellence in R&D (Grant No. SEV-2015-0522), the Catalan Agencia de Gestió d'Ajuts Universitaris i de Recerca (AGAUR) with SGR 2014–2016, Fundació Cellex Barcelona, the European Union's Horizon 2020 research and innovation program under Grant Agreement No. 654148 Laserlab-Europe, and Marie Skłodowska-Curie Grant Agreements No. 641272 and No. 264666. M.G.P. is supported by the ICFONEST program, partially funded by COFUND (FP7-PEOPLE-2013-COFUND), and B.W. was supported by AGAUR with a Ph.D. fellowship (Grant No. FI-DGR 2013–2015). X.W. was supported by the Chemical Sciences, Geosciences and Biosciences Division, Office of Basic Energy Sciences, Office of Science, US Department of Energy under Grant No. DE-FG02-86ER13491. X.-M.T. was supported by a Grand-in-Aid for Scientific Research (Grant No. C24540421) from the Japan Society for the Promotion of Science and the HA-PACS Project for advanced interdisciplinary computational sciences by exa-scale computing technology. We thank A.-T. Le and C.-D. Lin from the J. R. Macdonald Laboratory, Kansas State University, for their valuable theoretical input to this work.

[1] P. B. Corkum and F. Krausz, Nat. Phys. **3**, 381 (2007).
[2] T. Zuo, A. D. Bandrauk, and P. B. Corkum, Chem. Phys. Lett. **259**, 313 (1996).
[3] P. B. Corkum, Phys. Rev. Lett. **71**, 1994 (1993).
[4] M. G. Pullen, J. Dura, B. Wolter, M. Baudisch, M. Hemmer, N. Camus, A. Senftleben, C. D. Schroeter, R. Moshammer, J. Ullrich, and J. Biegert, J. Phys. B **47**, 204010 (2014).
[5] B. Wolter, C. Lemell, M. Baudisch, M. G. Pullen, X.-M. Tong, M. Hemmer, A. Senftleben, C. D. Schröter, J. Ullrich, R. Moshammer, J. Biegert, and J. Burgdörfer, Phys. Rev. A **90**, 063424 (2014).
[6] C. I. Blaga, F. Catoire, P. Colosimo, G. G. Paulus, H. G. Muller, P. Agostini, and L. F. DiMauro, Nat. Phys. **5**, 335 (2009).
[7] A. L'Huillier, L. A. Lompre, G. Mainfray, and C. Manus, Phys. Rev. Lett. **48**, 1814 (1982).
[8] S. Augst, D. D. Meyerhofer, D. Strickland, and S. L. Chin, J. Opt. Soc. Am. B **8**, 858 (1991).
[9] A. Rudenko, T. Ergler, K. Zrost, B. Feuerstein, V. L. B. de Jesus, C. D. Schröter, R. Moshammer, and J. Ullrich, Phys. Rev. A **78**, 015403 (2008).
[10] D. N. Fittinghoff, P. R. Bolton, B. Chang, and K. C. Kulander, Phys. Rev. A **49**, 2174 (1994).
[11] M. Kübel, K. J. Betsch, N. G. Kling, A. S. Alnaser, J. Schmidt, Y. Deng, I. Ben-Itzhak, G. G. Paulus, T. Pfeifer, J. Ullrich, R. Moshammer, M. F. Kling, and B. Bergues, New J. Phys. **16**, 033008 (2014).
[12] P. Kaminski, R. Wiehle, W. Kamke, H. Helm, and B. Witzel, Phys. Rev. A **73**, 013413 (2006).
[13] A. S. Alnaser, D. Comtois, A. T. Hasan, D. M. Villeneuve, J.-C. Kieffer, and I. V. Litvinyuk, J. Phys. B **41**, 031001 (2008).
[14] V. L. B. de Jesus, B. Feuerstein, K. Zrost, D. Fischer, A. Rudenko, F. Afaneh, C. D. Schröter, R. Moshammer, and J. Ullrich, J. Phys. B **37**, L161 (2004).
[15] C. Cornaggia and P. Hering, Phys. Rev. A **62**, 023403 (2000).
[16] J. L. Chaloupka, J. Rudati, R. Lafon, P. Agostini, K. C. Kulander, and L. F. DiMauro, Phys. Rev. Lett. **90**, 033002 (2003).
[17] R. Wiehle and B. Witzel, Phys. Rev. Lett. **89**, 223002 (2002).
[18] J. Rudati, J. L. Chaloupka, P. Agostini, K. C. Kulander, and L. F. DiMauro, Phys. Rev. Lett. **92**, 203001 (2004).
[19] Th. Weber, M. Weckenbrock, A. Staudte, L. Spielberger, O. Jagutzki, V. Mergel, F. Afaneh, G. Urbasch, M. Vollmer, H. Giessen, and R. Dörner, Phys. Rev. Lett. **84**, 443 (2000).
[20] T. Weber, H. Giessen, M. Weckenbrock, G. Urbasch, A. Staudte, L. Spielberger, O. Jagutzki, V. Mergel, M. Vollmer, and R. Dörner, Nature (London) **405**, 658 (2000).
[21] X. Sun, M. Li, D. Ye, G. Xin, L. Fu, X. Xie, Y. Deng, C. Wu, J. Liu, Q. Gong, and Y. Liu, Phys. Rev. Lett. **113**, 103001 (2014).
[22] G. Gingras, A. Tripathi, and B. Witzel, Phys. Rev. Lett. **103**, 173001 (2009).

[23] A. D. DiChiara, E. Sistrunk, C. I. Blaga, U. B. Szafruga, P. Agostini, and L. F. DiMauro, Phys. Rev. Lett. **108**, 033002 (2012).
[24] W. Kohn and L. J. Sham, Phys. Rev. **140**, A1133 (1965).
[25] X. M. Tong, G. Wachter, S. A. Sato, C. Lemell, K. Yabana, and J. Burgdörfer, Phys. Rev. A **92**, 043422 (2015).
[26] X. M. Tong and Shih-I. Chu, Phys. Rev. A **55**, 3406 (1997).
[27] X. M. Tong and Shih-I. Chu, Phys. Rev. A **57**, 452 (1998).
[28] X. M. Tong, K. Hino, and N. Toshima, Phys. Rev. A **74**, 031405(R) (2006).
[29] X. M. Tong, P. Ranitovic, C. W. Hogle, M. M. Murnane, H. C. Kapteyn, and N. Toshima, Phys. Rev. A **84**, 013405 (2011).
[30] P. Ranitovic, X. M. Tong, C. W. Hogle, X. Zhou, Y. Liu, N. Toshima, M. M. Murnane, and H. C. Kapteyn, Phys. Rev. Lett. **106**, 053002 (2011).
[31] M. V. Ammosov, N. B. Delone, and V. P. Krainov, Z. Eksp. Teor. Fiz. **91**, 2008 (1986) [Sov. Phys. JETP **64**, 1191 (1986)].
[32] X. M. Tong and C. D. Lin, J. Phys. B **38**, 2593 (2005).
[33] X. M. Tong, Z. X. Zhao, and C. D. Lin, Phys. Rev. A **66**, 033402 (2002).
[34] L. D. Landau and L. M. Lifshitz, *Quantum Mechanics (Non-relativistic Theory)*, 3rd ed. (Pergamon, 1977).
[35] C. Z. Bisgaard and L. B. Madsen, Am. J. Phys. **72**, 249 (2004).
[36] A. Thai, M. Hemmer, P. K. Bates, O. Chalus, and J. Biegert, Opt. Lett. **36**, 3918 (2011).
[37] B. Wolter, M. G. Pullen, M. Baudisch, M. Sclafani, M. Hemmer, A. Senftleben, C. D. Schröter, J. Ullrich, R. Moshammer, and J. Biegert, Phys. Rev. X **5**, 021034 (2015).
[38] J. Ullrich, R. Moshammer, A. Dorn, R. Dörner, L. P. H. Schmidt, and H. Schmidt-Böcking, Rep. Prog. Phys. **66**, 1463 (2003).
[39] S. M. Hankin, D. M. Villeneuve, P. B. Corkum, and D. M. Rayner, Phys. Rev. A **64**, 013405 (2001).
[40] B. Walker, B. Sheehy, L. F. DiMauro, P. Agostini, K. J. Schafer, and K. C. Kulander, Phys. Rev. Lett. **73**, 1227 (1994).
[41] M. G. Pullen, W. C. Wallace, D. E. Laban, A. J. Palmer, G. F. Hanne, A. N. Grum-Grzhimailo, K. Bartschat, I. Ivanov, A. Kheifets, D. Wells, H. M. Quiney, X. M. Tong, I. V. Litvinyuk, R. T. Sang, and D. Kielpinski, Phys. Rev. A **87**, 053411 (2013).
[42] M. G. Pullen, B. Wolter, A.-T. Le, M. Baudisch, M. Hemmer, A. Senftleben, C. D. Schröter, J. Ullrich, R. Moshammer, C. D. Lin, and J. Biegert, Nat. Commun. **6**, 7262 (2015).
[43] B. Gaire, S. Y. Lee, D. J. Haxton, P. M. Pelz, I. Bocharova, F. P. Sturm, N. Gehrken, M. Honig, M. Pitzer, D. Metz, H.-K. Kim, M. Schoffler, R. Dorner, H. Gassert, S. Zeller, J. Voigtsberger, W. Cao, M. Zohrabi, J. Williams, A. Gatton, D. Reedy, C. Nook, T. Muller, A. L. Landers, C. L. Cocke, I. Ben-Itzhak, T. Jahnke, A. Belkacem, and Th. Weber, Phys. Rev. A **89**, 013403 (2014).
[44] Y. H. Jiang, A. Senftleben, M. Kurka, A. Rudenko, L. Foucar, O. Herrwerth, M. F. Kling, M. Lezius, J. V. Tilborg, A. Belkacem, K. Ueda, D. Rolles, R. Treusch, Y. Z. Zhang, Y. F. Liu, C. D. Schröter, J. Ullrich, and R. Moshammer, J. Phys. B **46**, 164027 (2013).
[45] B. Wolter, M. G. Pullen, A.-T. Le, M. Baudisch, K. Doblhoff-Dier, A. Senftleben, M. Hemmer, C. Dieter Schröter, J. Ullrich, T. Pfeifer, R. Moshammer, S. Gräfe, O. Vendrell, C. D. Lin, and J. Biegert, Science **354**, 308 (2016).